Applied Catalysis B: Environmental 162 (2015) 204–209

Contents lists available at ScienceDirect

Applied Catalysis B: Environmental

journal homepage: www.elsevier.com/locate/apcatb

Selective photocatalytic decomposition of formic acid over AuPd nanoparticle-decorated TiO_2 nanofibers toward high-yield hydrogen production

Zhenyi Zhang[a,b], Shao-Wen Cao[b], Yusen Liao[b], Can Xue[b,*]

[a] School of Physics and Materials Engineering, Dalian Nationalities University, Dalian 116600, PR China
[b] Solar Fuels Laboratory, School of Materials Science and Engineering, Nanyang Technological University, 50 Nanyang Avenue, Singapore 639798, Singapore

ARTICLE INFO

Article history:
Received 1 April 2014
Received in revised form 18 June 2014
Accepted 30 June 2014
Available online 7 July 2014

Keywords:
Photocatalysis
AuPd alloy
Electrospinning
Surface plasmon resonance
Formic acid decomposition

ABSTRACT

We present high-yield hydrogen production through selective photocatalytic decomposition of formic acid by using electrospun TiO_2 nanofibers decorated with AuPd bimetallic alloy nanoparticles under simulated sunlight irradiation. By using only 5 mg of the AuPd/TiO_2 nanofibers containing the 0.75% Au and 0.25% Pd, we could achieve an optimal H_2 generation rate of 88.5 μmol h^{-1} with an apparent quantum yield at 365 nm as 15.6%, which is higher than that of the Pd/TiO_2 and Au/TiO_2 nanofibers by a factor of 1.6 and 4.5, respectively. The enhanced photocatalytic decomposition of formic acid for H_2 generation could be attributed to the stronger electron-sink effect of AuPd alloy nanoparticles, the high selectivity of Pd for the dehydrogenation of formic acid, and the surface plasmon resonance effect of Au. More importantly, we demonstrate that the photocatalytic processes enable re-activation of the AuPd nanoparticles that were poisoned by CO during thermal decomposition of formic acid. As such, the presented AuPd/TiO_2 nanofibers are promising materials for re-generation of H_2 under mild conditions from liquid storage carrier of hydrogen.

1. Introduction

The worldwide problem of air pollution induced by the excessive use of fossil fuels has become increasingly serious issues for human beings in modern society. Hydrogen gas has been recognized as one of clean and renewable energy sources to replace fossil fuels for the sustainable future [1,2]. However, the extremely low density and highly explosive character of hydrogen gas lead to significant challenges in its storage and transportation [3]. Recently, considerable attentions have been received on the liquid phase storage of hydrogen by using solutions of small molecules that are capable of controllable H_2 releasing in mild conditions [4–6]. In particular, formic acid (FA), as a non-toxic and non-flammable matter, contains 4.4% (w/w) of hydrogen and has been considered as a promising hydrogen source because the FA decomposition into H_2 and CO_2 ($HCOOH \rightarrow H_2 + CO_2$) is thermodynamically favored ($\Delta G = -32.8\ kJ\ mol^{-1}$). However, a competitive route of FA decomposition into CO and H_2O ($\Delta G = -20.7\ kJ\ mol^{-1}$) usually occurs, which is undesirable [7–9]. Therefore, the major challenge of exploiting FA as a practical carrier of hydrogen is finding suitable catalysts that enable highly selective FA decomposition into H_2/CO_2 rather than CO/H_2O to occur with high efficiency and large throughput in ambient condition.

To date, many researchers have explored the potentials of photocatalytic decomposition of FA for H_2 production by using different semiconductors (e.g. TiO_2, CdS, Cu_2O, etc.) though it often led to poor selectivity in the FA decomposition process with high CO concentration in the product [10–12]. In addition, to enhance the photocatalytic efficiency, people usually deposit noble metal (e.g. Pt, Pd, Au) nanoparticles that promote the separation of photogenerated charge carriers [13–16]. In particular, Pd nanoparticles have been reported to have high activity and selectivity for the FA decomposition at near-ambient temperatures [17–20]. However, the existence of CO in the gaseous product can cause poisoning of Pd, leading to the deactivation of the metal catalysts during the FA decomposition process [18,21,22]. Recently, researchers found that Pd-based alloy catalysts may overcome the poisoning and improve the selectivity to enhance the H_2 production from FA decomposition [21–23]. Among the various bimetallic alloy materials, AuPd alloy nanoparticles are especially attractive due to their excellent catalytic activity and high stability [21–25]. Furthermore, the surface plasmon resonance (SPR) of Au may provide

* Corresponding author. Tel.:+65 6790 6180; fax: +65 6790 9081.
E-mail address: cxue@ntu.edu.sg (C. Xue).

http://dx.doi.org/10.1016/j.apcatb.2014.06.055
0926-3373/

additional enhancement on the photocatalytic activity when the AuPd nanoparticles are conjugated with the semiconductor structures.

Herein, we report highly selective photocatalytic FA decomposition toward high-yield H_2 production by using AuPd nanoparticle-decorated TiO_2 nanofibers fabricated by a facile electrospinning technique. The electrospun nanofibrous materials have been known as excellent structures for catalytic applications due to the three-dimensional (3D) open structure, large surface areas, and high porosity. Under simulated sunlight (AM 1.5 sunlight, 100 mW cm^{-2}) irradiation, the H_2 production rate of the optimal composite nanofibers containing 0.75% Au and 0.25% Pd could reach 88.5 μmol h^{-1}, which was about 1.6 and 4.5 times higher than that of Pd/TiO_2 and Au/TiO_2 nanofibers, respectively. The higher activity of AuPd/TiO_2 nanofibers for H_2 production through photocatalytic FA decomposition might be attributed to the high selectivity of Pd for the FA dehydrogenation, stronger electron-sink effect of AuPd nanoparticles and the surface plasmon resonance (SPR) effect of Au.

2. Experiments

2.1. Fabrication of Au–Pd/TiO_2 composite nanofibers

The AuPd/TiO_2 nanofibers were fabricated via electrospinning followed by calcination. Typically, 2.0 mL tetrabutyl titanate ($Ti(OC_4H_9)_4$) and a certain amount of $Pd(C_2H_3O_2)_2$ were added to a mixture solution containing of 2 mL acetic acid and 5 mL ethanol under vigorous stirring. Then, 0.4 g poly(vinyl pyrrolidone) (PVP) powder (Mn = 1300,000) were dissolved in the above solution followed by stirring for 3 h. Subsequently, a certain amount of $HAuCl_4$ was added to this solution which was kept stirring for another 6 h and used as the precursor solution of PVP/$HAuCl_4$/$Pd(C_2H_3O_2)_2$/$Ti(OC_4H_9)_4$. Afterward, this precursor solution was transferred into a plastic syringe with a stainless steel needle (23-ga) for electrospinning. The distance between the needle tip and the collector was about 15 cm, and the feeding rate was 2.0 mL h^{-1}. The dense web of PVP/$HAuCl_4$/$Pd(C_2H_3O_2)_2$/$Ti(OC_4H_9)_4$ nanofibers was generated at an applied electric voltage of 15 kV between the needle tip and the collector, followed by calcination in air at 500 °C for 2 h (ramping rate of 2 °C min^{-1}) to get the final AuPd/TiO_2 nanofibers.

The Pd_1/TiO_2 nanofibers (1% Pd in mole fraction) were synthesized via photodeposition of Pd onto electrospun TiO_2 nanofibers. Briefly, quantitative $Pd(C_2H_3O_2)_2$ (1% mole ratio to Ti) and TiO_2 nanofibers (20 mg) were added into a mixed solution of 14 mL deionized water, 4 mL ethanol and 2 mL acetic acid. Then, this suspension was exposed under UV–vis light (300-W xenon lamp) for 20 min to deposit Pd nanoparticles onto the TiO_2 nanofibers. Then the nanofibers were collected via centrifugation, washed with deionized water and ethanol for several times, and finally dried in an electric oven at 80 °C for 4 h.

2.2. Characterization

X-ray diffraction (XRD) measurements were carried out on a Shimadzu XRD-600 X-ray diffractometer with a Cu *K*α line of 0.1541 nm. X-ray photoelectron spectroscopy (XPS) was performed on a Thermo Scientific Theta probe XPS with monochromatized Al *K*α ($h\nu$ = 1486.7 eV) source. Field emission scanning electron microscopy (FESEM; JSM-7600F) and transmission electron microscopy (TEM; JEOL JEM-2100) were used to characterize the morphologies and structures of the products. Energy dispersive X-ray (EDX) spectroscopy being attached to SEM and TEM was used to analyze the composition of products. UV–vis diffuse reflectance spectra were recorded on a Lambda 750 UV/vis/NIR spectrophotometer (Perkin Elmer, USA). The photoluminescence (PL) spectra were recorded on a Shimazu RF-5310PC fluorophotometer.

2.3. Photocatalytic decomposition of formic acid

The photocatalytic tests were performed in a 40 mL quartz reactor. Typically, 5 mg of the as-electrospun nanofiber photocatalysts were suspended in 10 mL aqueous solution of formic acid aqueous solution (2.7 M). The above suspension was sealed in the quartz reactor by a rubber plug, and then purged with nitrogen gas for half an hour to drive away the residual oxygen. Finally, the reactor loading with the suspension was exposed under the simulated sunlight irradiation by using a solar simulator (67005, Newport Corp.) with a measured intensity equivalent to standard AM 1.5 sunlight (100 mW cm^{-2}). The gas products composition from the upper space above the liquid suspension in the quartz reactor were periodically analyzed quantitatively by an Agilent 7890A gas chromatograph (GC) equipped with a thermal conductivity detector (TCD).

2.4. Photocurrent measurement

The photocurrent responses of the samples were tested by using an electrochemical analyzer (CHI 660D, CH Instruments Inc.) in a three-electrode system. Pt wire and Ag/AgCl were employed as the counter and reference electrode, respectively. For the working electrode preparation, the prepared nanofibers (5 mg) were mixed with 0.1 mL deionized water and 0.01 mL Triton X-100 to form a paste, which was then coated onto a F-doped SnO_2 (FTO) glass with an effective area of 1 cm × 1 cm and followed by calcination at 450 °C for 2 h. Before irradiation, the electrolyte solution (2.7 M formic acid) was degassed by purging N_2 gas for 20 min. Then, the as-prepared working electrode was irradiated by a solar simulator (67005, Newport Corp.) with a measured intensity equivalent to standard AM 1.5 sunlight (100 mW cm^{-2}).

3. Results and discussion

The Au–Pd/TiO_2 nanofibers with different mole fractions of Au and Pd were fabricated by electrospinning the precursor solution consisting of $HAuCl_4$, $Pd(C_2H_3O_2)_2$, tetrabutyl titanate ($Ti(OC_4H_9)_4$) and poly(vinylpyrrolidone) (PVP), followed by thermal decomposition for removal of the polymers (Fig. S1). The products are denoted as Au_xPd_{1-x}/TiO_2 nanofibers, in which *x* is the molar concentration (*x*%) of Au to Ti in the precursor solution. Fig. 1A showed the X-ray diffraction (XRD) pattern of the prepared nanofibers of TiO_2, Au_1/TiO_2, $Au_{0.75}Pd_{0.25}$/TiO_2 and the control sample Pd_1/TiO_2 prepared by photo-deposition of Pd nanoparticles over TiO_2 nanofibers because the post calcination process after electronspinning could not create Pd nanoparticles from the Pd^{2+} precursors. The diffraction peaks for all products could be indexed as the tetragonal anatase TiO_2 (JCPDS, no. 21-1272). The enlarged view of XRD patterns (from 35 to 55°) revealed the presence of face-centered cubic (fcc) Au nanocrystals (JCPDS, no. 04-0784) in the Au_1/TiO_2 nanofibers. But the diffraction peaks of Pd nanocrystals were hardly observable in the XRD pattern of Pd_1/TiO_2 nanofibers, which might be due to the low crystallinity of very small Pd nanoparticles (Fig. S2). In the case of $Au_{0.75}Pd_{0.25}$/TiO_2 nanofibers, the diffraction peaks of metal nanocrystals exhibit slight shift as compared to that of typical fcc Au, indicating the formation of AuPd alloy in the TiO_2 matrix. The scanning electron microscopy (SEM) images (Fig. 1B) showed that the prepared electrospun nanofibers had an average diameter of 200 ± 20 nm and very large length (up to 20 μm) with random orientations. The analysis by energy-dispersive X-ray (EDX) spectroscopy from the corresponding transmission electron microscopy

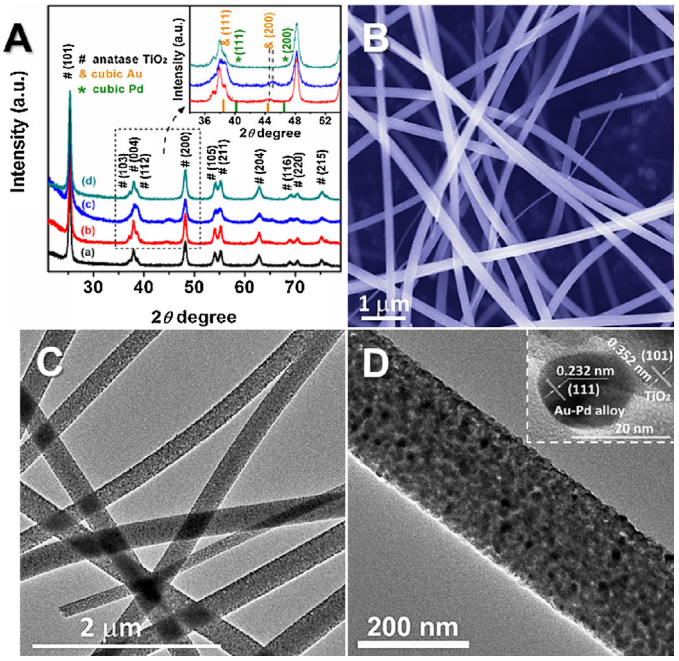

Fig. 1. (A) XRD patterns of the as-electrospun nanofibers: (a) TiO_2; (b) Au_1/TiO_2; (c) $Au_{0.75}Pd_{0.25}/TiO_2$; (d) Pd_1/TiO_2; (B) SEM and ((C) and (D)) TEM images of the $Au_{0.75}Pd_{0.25}/TiO_2$ nanofibers; The inset shows the corresponding HRTEM image.

(TEM) image confirmed that the element contents of Au and Pd in the as-electrospun $Au_{0.75}Pd_{0.25}/TiO_2$ sample were very close to the theoretical value in the precursor solution for electrospinning (Fig. S3). As observed in Fig. 1D, the AuPd nanoparticles with an average diameter of 13.8 nm are well-dispersed in the TiO_2 Nanofibers matrix. The lattice fringes of fcc AuPd alloy and anatase TiO_2 could be clearly observed in the high resolution TEM (HRTEM) image (insert of Fig. 1D) of the $Au_{0.75}Pd_{0.25}/TiO_2$ nanofibers.

In order to further verify the formation of AuPd alloy nanoparticles in the TiO_2 nanofibers, the Au_1/TiO_2 and $Au_{0.75}Pd_{0.25}/TiO_2$ samples were examined by X-ray photoelectron spectroscopy (XPS). As shown in Fig. 2, the Au $4f_{7/2}$ and Au $4f_{5/2}$ peaks in the spectrum of $Au_{0.75}Pd_{0.25}/TiO_2$ nanofibers locate at 83.5 and 87.3 eV, respectively, which exhibit slight upshift as compared to that of Au_1/TiO_2 nanofibers [13,15]. In addition, the Pd 3d core-level spectra of $Au_{0.75}Pd_{0.25}/TiO_2$ nanofibers could be fitted into

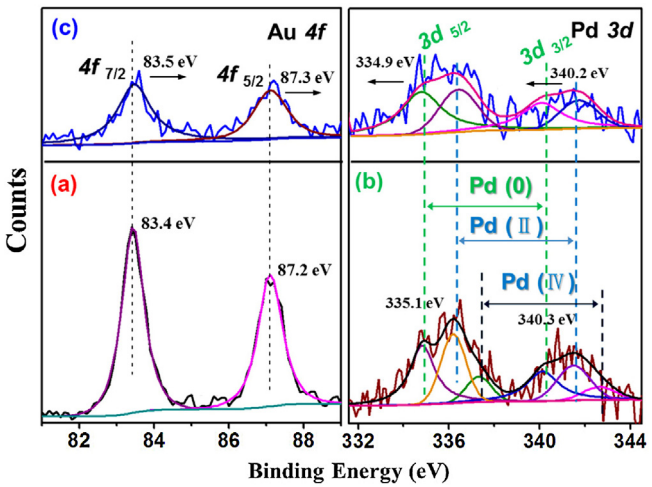

Fig. 2. XPS spectra of the (a) Au_1/TiO_2; (b) Pd_1/TiO_2; (c) $Au_{0.75}Pd_{0.25}/TiO_2$ nanofibers, showing the binding energy of Au 4f core-level (left) and Pd 3d core-level (right).

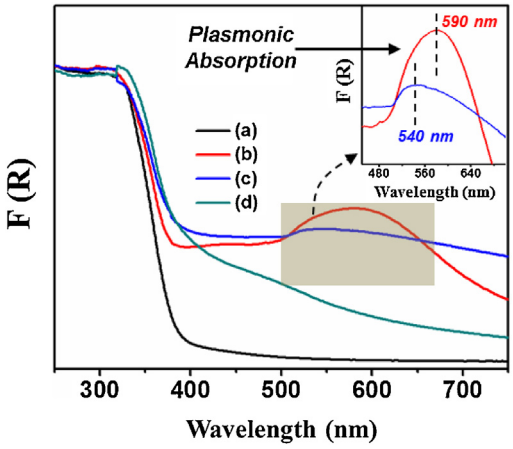

Fig. 3. UV–vis absorption spectra of the as-electrospun nanofibers: (a) TiO_2; (b) Au_1/TiO_2; (c) $Au_{0.75}Pd_{0.25}/TiO_2$; (d) Pd_1/TiO_2 nanofibers.

four symmetric peaks, suggesting the existence of two states of Pd species. The Pd $3d_{5/2}$ peak at 334.9 eV and Pd $3d_{3/2}$ peak at 340.2 eV are attributed to the metallic Pd^0, while the binding energy peaks shown at 336.1 and 341.5 eV are originated from $3d_{5/2}$ and $3d_{3/2}$ of Pd^{2+}, respectively [26]. This result indicated that the oxide was present on the surface of the Pd. Note that the binding energy peaks of Pd 3d on the curve of $Au_{0.75}Pd_{0.25}/TiO_2$ nanofibers showed a slight downshift relative to the Pd 3d peaks appeared on the curves Pd_1/TiO_2 nanofibers. The shift of the binding energy for Au and Pd in the $Au_{0.75}Pd_{0.25}/TiO_2$ nanofibers could be ascribed to the charge transfer between them due to the formation of AuPd alloy [27].

Fig. 3 shows the UV–vis absorption spectra of the prepared samples, which were converted from the measured diffuse reflectance spectra by using the Kubelka–Munk function. The intense UV absorption band below 400 nm could be assigned to the intrinsic bandgap absorption of anatase TiO_2 (E_g: ~3.2 eV) [28]. Comparing with pure TiO_2 nanofibers, the Au_1/TiO_2 nanofibers exhibited a clear absorption band centered at ~590 nm that could be attributed to the surface plasmon resonance (SPR) of Au [15], while the Pd_1/TiO_2 nanofibers did not exhibit clear SPR signatures in the absorption spectrum. For the $Au_{0.75}Pd_{0.25}/TiO_2$ nanofibers, the Au SPR peak exhibited a blue-shift to 540 nm with decreased intensity, which could be ascribed to the increase of electron density in Au particle upon forming alloy with Pd [29].

The tests of photocatalytic formic acid decomposition over the electrospun nanofibers were carried out under simulated sunlight irradiation (100 mW cm^{-2}). Fig. 4A showed the amount of H_2 production over different samples as a function of irradiation time. The pure TiO_2 nanofibers showed a very low H_2 generation rate (4.0 μmol h^{-1}), which could be ascribed to the fast recombination of photogenerated charge carriers and the high overpotential for H_2 evolution on TiO_2 surfaces. In comparison, the H_2 production rates of Au_1/TiO_2 and Pd_1/TiO_2 nanofibers were about 19.5 and 54.5 μmol h^{-1}, respectively. This indicated that the metallic Au or Pd nanoparticles could act as electron sinks to hold the photogenerated electrons from excited TiO_2, and serve as active sites for FA dehydrogenation into hydrogen gas. Further, the higher H_2 generation rate on Pd_1/TiO_2 nanofibers than on the Au_1/TiO_2 nanofibers can be attributed to the two aspects: (1) Pd has higher activity for FA dehydrogenation as compared to Au [17–20]; (2) co-catalytic effect due to the larger work function of Pd (5.2 eV) than that of Au (5.1 eV) [30]. Notably, as shown in Fig. 4D, the TiO_2 nanofibers decorated with AuPd alloy nanoparticles shower even higher H_2 generation rate. In particular, the H_2 production rate of $Au_{0.75}Pd_{0.25}/TiO_2$ nanofibers could reach 88.5 μmol h^{-1}, which was about 1.6 times higher than that of Pd_1/TiO_2. However, under visible light

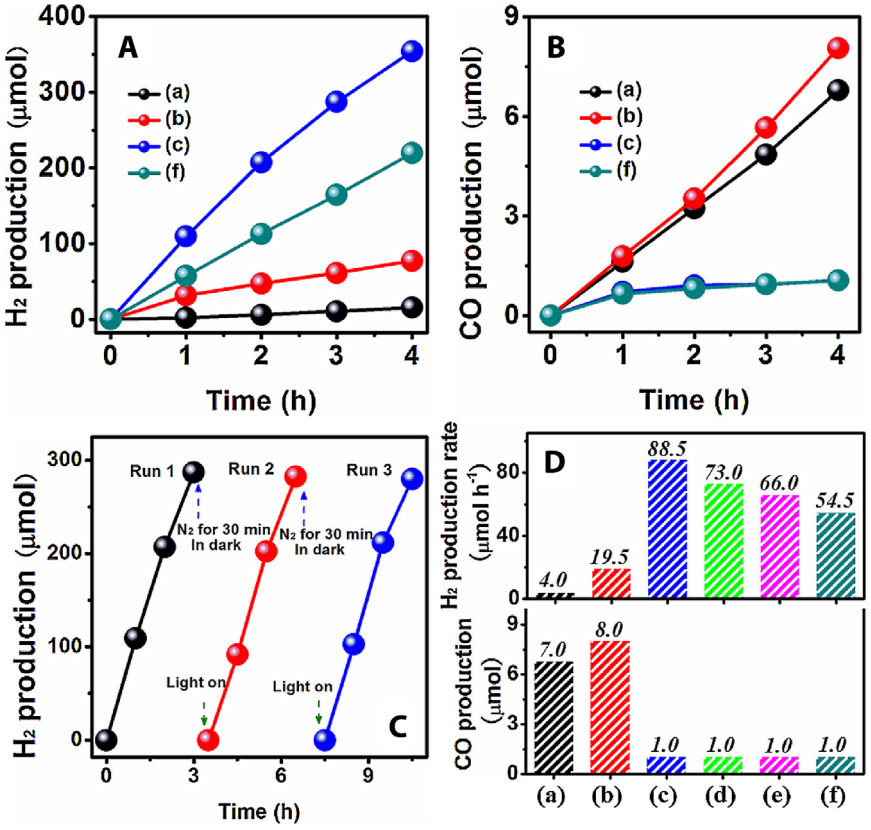

Fig. 4. Results of photocatalytic formic acid decomposition under simulated sunlight irradiation over different nanofibers: (a) TiO_2; (b) Au_1/TiO_2; (c) $Au_{0.75}Pd_{0.25}/TiO_2$; (d) $Au_{0.5}Pd_{0.2}/TiO_2$, (e) $Au_{0.25}Pd_{0.75}/TiO_2$; (f) Pd_1/TiO_2 nanofibers. (A) photocatalytic H_2 production amount versus irradiation time; (B) photocatalytic CO production amount versus irradiation time; (C) cycling test of photocatalytic H_2 production over the $Au_{0.75}Pd_{0.25}/TiO_2$ nanofibers; (D) H_2 production rates and CO production amounts (after 4 h).

irradiation (λ: 420–780 nm), no appreciable hydrogen production was observed over the $Au_{0.75}Pd_{0.25}/TiO_2$ nanofibers, indicating that the hydrogen production from photocatalytic decomposition of formic acid is mainly caused by the TiO_2 excitation. Moreover, the cycling test over $Au_{0.75}Pd_{0.25}/TiO_2$ nanofibers for 9 h (Fig. 4C) showed steady H_2 production rate after three cycles, indicating very stability of the sample in the photocatalytic FA decomposition process. The apparent quantum efficiency (QE) could be estimated as ~15.6% at 365 nm (see Supporting information). The higher activity for H_2 evolution might be attributed to more efficient FA dehydrogenation over AuPd alloy surfaces [21,22,26].

In addition, the AuPd alloy nanoparticles may provide stronger electron-sink effect that increases the photocatalytic activity. To prove this, we carried out photoelectrochemical tests (Fig. 5) in formic acid solution by using the prepared nanofibers. It was found that the dark currents were very low for all the nanofibers while their anodic photocurrents could be clearly observed under simulated sunlight irradiation. As shown in Fig. 5, the $Au_{0.75}Pd_{0.25}/TiO_2$ nanofibers showed the highest photocurrent density as compared with the other nanofibers, suggesting promoted charge separation from the excitation of the TiO_2 matrix by the decorated AuPd alloy nanoparticles. The stronger electron-sink effect of Au–Pd alloy nanoparticles is also supported by the comparison of photoluminescence (PL) spectra of these nanofibers (Fig. S4). The $Au_{0.75}Pd_{0.25}/TiO_2$ nanofibers exhibited obviously lower PL intensity than other samples, suggesting that more efficient transfer of photogenerated electrons from TiO_2 to the AuPd nanoparticles in these nanofibers.

The selectivity of FA decomposition for H_2 production can be identified by comparing the CO generation rate. As shown in Fig. 4B and D, all samples containing Pd exhibit very low CO generation rate (<1.0 μmol h^{-1}), which is about 7 and 8 times lower than that of TiO_2 and Au_1/TiO_2 nanofibers, respectively. This observation indicates that the Pd or AuPd alloy surfaces provide very high selectivity for FA dehydrogenation for H_2 evolution as opposed to FA dehydration for CO generation. It was generally known that the CO molecules could adsorb on the surface of Pd and reduce its catalytic activity [3,18,21,22]. However, interestingly, in the present condition, the metal particles were not poisoned by the produced CO gas, suggesting that the light irradiation might prevent poisoning by CO or re-activate the CO-poisoned Pd.

To verify this hypothesis, we carried out FA decomposition at 80 °C without light irradiation by using the $Au_{0.75}Pd_{0.25}/TiO_2$ nanofibers as the catalyst. As shown in Fig. 6, at the beginning,

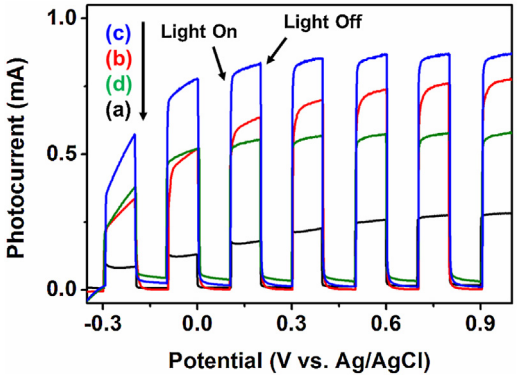

Fig. 5. Chopped *I–V* curves of the electrospun nanofibers: (a) TiO_2; (b) Au_1/TiO_2; (c) $Au_{0.75}Pd_{0.25}/TiO_2$; (d) Pd_1/TiO_2 nanofibers.

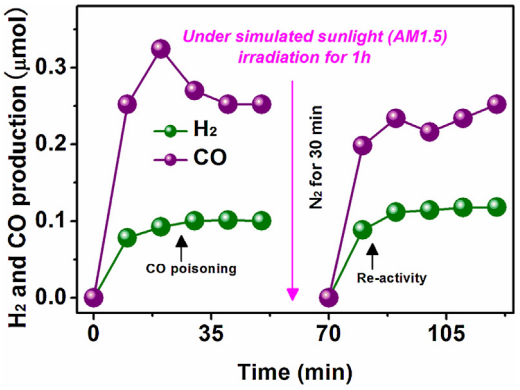

Fig. 6. H_2 and CO production amount versus reaction time over the $Au_{0.75}Pd_{0.25}/TiO_2$ nanofibers at 80 °C without light irradiation.

the catalyst was active for the FA decomposition, and both H_2 and CO evolution could be observed. However, the gas evolution rate decreased after 10 min, and the reaction stopped after 30 min due to the CO-poisoning on the AuPd surfaces. Interestingly, after we irradiated the reaction suspension with simulated sunlight for 1 h and purged the reactor with N_2 for 30 min, the thermal FA decomposition at 80 °C without light irradiation occurred again with similar gas evolution rate at the first 10 min and stopped again after 30 min. This observation demonstrated that the CO-poisoned metal surface can be re-activated through light excitation of the contacted TiO_2 matrix. However, under visible light irradiation (λ: 420–780 nm), the re-activation of AuPd/TiO_2 nanofibers could not occur.

The re-activation mechanism might be explained by the following processes. First, under light irradiation, the photogenerated electrons in the TiO_2 conduction band can transfer to the AuPd nanoparticles, whereas the photogenerated holes remain in the valence band due to the electron-sink effect as aforementioned. As such, the photogenerated holes can be trapped by surface hydroxyl groups of TiO_2 to yield hydroxyl radicals (OH•) that could oxidize the CO adsorbed at the interfaces of TiO_2 and AuPd nanoparticles. The presence of OH• may be proved by the test shown in Fig. S5. Second, the residual oxygen in the reaction system could be adsorbed on the AuPd surfaces and react with the photogenerated electrons to form superoxide radical anions ($O_2•^-$) as well as hydroperoxy radicals ($HO_2•$) and hydroxyl radical (OH•) upon protonation [31,32]. These radicals are able to oxidize the CO adsorbed on the AuPd surface to form the CO_2 [33], leading to the re-activation of AuPd nanoparticles.

It is noteworthy pointing out that among these AuPd/TiO_2 nanofibers, the $Au_{0.75}Pd_{0.25}/TiO_2$ possessed the highest H_2 production rate. Even though Pd is a better catalyst for FA dehydrogenation than Au, the higher Pd content in the nanofibers did not result in higher H_2 generation rate. From the UV–vis absorption spectra (Fig. S6), we could observe a clear Au SPR band for the $Au_{0.75}Pd_{0.25}/TiO_2$ nanofibers while the other two samples, $Au_{0.5}Pd_{0.5}/TiO_2$ and $Au_{0.25}Pd_{0.75}/TiO_2$ could not show distinguishable SPR band from the Au. Therefore, the SPR effect of Au might also provide enhancement to the photocatalytic activity of the AuPd/TiO_2 nanofibers [34]. In order to verify the contribution of SPR for FA dehydrogenation, we carried out a 2-h photocatalytic tests by using the $Au_{0.75}Pd_{0.25}/TiO_2$ nanofibers under dual-beam irradiation, in which one beam at 365 ± 10 nm for TiO_2 excitation and a secondary beam at 550 ± 20 nm for Au SRP excitation. As shown in Fig. S7, comparing to the H_2 production amount under single irradiation at 365 ± 10 nm, a simultaneous secondary irradiation at 550 ± 20 nm led to an enhanced H_2 generation amount by about 1.12 times, while the single irradiation at 550 ± 20 nm could not result in observable H_2 evolution. This observation demonstrated that when the TiO_2 matrix is excited for FA decomposition, the simultaneous SPR excitation of Au in the $Au_{0.75}Pd_{0.25}/TiO_2$ nanofibers could provide additional enhancement for the photocatalytic process, which might be attributed to the involvement of hot plasmonic electrons in FA decomposition and the promoted electron–hole separation in the TiO_2 matrix near the Au or AuPd nanoparticles.

4. Conclusion

In summary, the high-yield H_2 production was achieved through photocatalytic formic acid decomposition by using the electrospun AuPd/TiO_2 nanofibers as the photocatalysts under simulated sunlight irradiation. The optimal nanofibers photocatalyst with 0.75 at.% Au and 0.25 at.% Pd displayed a high selectivity of H_2 production with the rate of 88.5 μmol h^{-1}, which was about 22 times higher than the rate of pure TiO_2 nanofibers, and exceeded the rates of Pd_1/TiO_2 and Au_1/TiO_2 nanofibers by a factor of 1.6 and 4.5, respectively. The high photoactivity of AuPd/TiO_2 nanofibers for the H_2 production through decomposition of FA might be attributed to the high selectivity of Pd for the dehydrogenation reaction, the strong electron-sink effect of AuPd NPs, and the SPR effect of Au. We also found that the photocatalytic processes enable re-activation of the AuPd nanoparticles that were poisoned by CO during thermal decomposition of formic acid. This work offers a new strategy to obtain the high-yield H_2 production at ambient condition with solar irradiation, and provides a useful platform for the development of solar-to-fuel energy conversion.

Acknowledgments

This work was financially supported by NTU seed funding for Solar Fuels Laboratory, MOE AcRF-Tier1 RG 44/11, MOE AcRF-Tier2 (MOE2012-T2-2-041, ARC 5/13), and CRP program (NRF-CRP5-2009-04) from the Singapore National Research Foundation (NRF). Z. Y. Zhang thanks the support from the National Basic Research Program of China (973 Program) (Grant No. 2012CB626801), National Natural Foundation of China (Grant No. 11274057), and Scientific Research Foundation for Doctor of Liaoning Province (Grant No. 20141118).

Appendix A. Supplementary data

Supplementary data associated with this article can be found, in the online version, at http://dx.doi.org/10.1016/j.apcatb.2014.06.055.

References

[1] S. Park, J.M. Vohs, R.J. Gorte, Nature 404 (2000) 265–267.
[2] K. Shimura, H. Yoshida, Energy Environ. Sci. 4 (2011) 2467–2481.
[3] M. Grasemann, G. Laurenczy, Energy Environ. Sci. 5 (2012) 8171–8181.
[4] T.C. Johnson, D.J. Morris, M. Wills, Chem. Soc. Rev. 39 (2010) 81–88.
[5] R.M. Navarro, M.C. Sánchez-Sánchez, M.C. Alvarez-Galvan, F. Valle, J.L.G. Fierro, Energy Environ. Sci. 2 (2009) 35–54.
[6] K. Ohkubo, K. Mizushima, R. Iwata, S. Fukuzumi, Chem. Sci. 2 (2011) 715–722.
[7] P.G. Jessop, The Handbook of Homogeneous Hydrogenation, Wiley-VCH Verlag GmbH, Weinheim, 2008, pp. 489–511.
[8] I. Ntaikou, H.N. Gavala, M. Kornaros, G. Lyberatos, Int. J. Hydrogen Energy 33 (2008) 1153–1163.
[9] F. Joó, ChemSusChem 1 (2008) 805–808.
[10] M.A. Henderson, J. Phys. Chem. B 101 (1997) 221–229.
[11] H.J. Yun, H. Lee, J.B. Joo, W. Kim, J. Yi, J. Phys. Chem. C 113 (2009) 3050–3055.
[12] M. Matsumura, M. Hiramoto, T. Iehara, H. Tsubomura, J. Phys. Chem. 88 (1984) 248–250.
[13] Z. Zhang, Z. Wang, S.W. Cao, C. Xue, J. Phys. Chem. C 117 (2013) 25939–25947.
[14] Y. Wei, S. Han, D.A. Walker, S.C. Warren, B.A. Grzybowski, Chem. Sci. 3 (2012) 1090–1094.
[15] Z.Y. Zhang, A. Li, S.W. Cao, M. Bosman, S. Li, C. Xue, Nanoscale 6 (2014) 5217–5222.
[16] G. Halasi, G. Schubert, F. Solymosi, J. Phys. Chem. C 116 (2012) 15396–15405.
[17] M. Yadav, A.K. Singh, N. Tsumori, Q. Xu, J. Mater. Chem. 22 (2012) 19146–19150.

[18] D. Zhou, L. Ding, H. Cui, H. An, J. Zhai, Q. Li, J. Power Sources 222 (2013) 510–517.
[19] Y. Sugano, K. Fujiwara, Y. Shiraishi, S. Ichikawa, T. Hirai, Catal. Sci. Technol. 3 (2013) 1718–1724.
[20] N. Zhang, S. Liu, X. Fu, Y.-J. Xu, J. Mater. Chem. 22 (2012) 5042–5052.
[21] Y. Huang, X. Zhou, M. Yin, C. Liu, W. Xing, Chem. Mater. 22 (2010) 5122–5128.
[22] X. Zhou, Y. Huang, W. Xing, C. Liu, J. Liao, T. Lu, Chem. Commun. 30 (2008) 3540–3542.
[23] R. Su, R. Tiruvalam, A.J. Logsdail, Q. He, C.A. Downing, M.T. Jensen, N. Dimitratos, L. Kesavan, P.P. Wells, R. Bechstein, H.H. Jensen, S. Wendt, C.R.A. Catlow, C.J. Kiely, G.J. Hutchings, F. Besenbacher, ACS Nano 8 (2014) 3490–3497.
[24] Y. Mizukoshi, K. Sato, T.J. Konno, N. Masahashi, Appl. Catal., B: Environ. 94 (2010) 248–253.
[25] X. Yang, C. Huang, Z.Y. Fu, H.Y. Song, S.J. Liao, Y.L. Su, L. Du, X.J. Li, Appl. Catal., B: Environ. 140 (2013) 419–425.
[26] G. Zhang, Y. Wang, X. Wang, Y. Chen, Y. Zhou, Y. Tang, L. Lu, J. Bao, T. Lu, Appl. Catal., B: Environ. 102 (2011) 614–619.
[27] C. Xu, R. Wang, M. Chen, Y. Zhang, Y. Ding, Phys. Chem. Chem. Phys. 12 (2010) 239–246.
[28] A.L. Linsebigler, G. Lu, J.T. Yates, Chem. Rev. 95 (1995) 735–758.
[29] P. Mulvaney, M. Giersig, A. Henglein, J. Phys. Chem. 96 (1992) 10419–10424.
[30] Y. Mizukoshi, Y. Makise, T. Shuto, J. Hu, A. Tominaga, S. Shironita, S. Tanabe, Ultrason. Sonochem. 14 (2007) 387–392.
[31] T. Aarthi, G. Madras, Ind. Eng. Chem. Res. 46 (2007) 7–14.
[32] K. Rajeshwar, M.E. Osugi, W. Chanmanee, C.R. Chenthamarakshan, M.V.B. Zanoni, P. Kajitvichyanukul, R. Krishnan-Ayer, J. Photochem. Photobiol., C: Photochem. Rev. 9 (2008) 171–192.
[33] S. Roy, M.S. Hegde, N. Ravishankar, G. Madras, J. Phys. Chem. 111 (2007) 8153–8160.
[34] J. Fang, S.W. Cao, Z. Wang, M.M. Shahjamali, F. Boey, S.C.J. Loo, J. Barber, C. Xue, Int. J. Hydrogen Energy 37 (2012) 17853–17861.